Available online at www.sciencedirect.com
ScienceDirect
Russian Geology and Geophysics 58 (2017) 1289–1304
RUSSIAN GEOLOGY AND GEOPHYSICS
www.elsevier.com/locate/rgg

Mantle heterogeneity at the Bouvet triple junction based on the composition of olivine phenocrysts

N.A. Migdisova [a,*], A.V. Sobolev [a,b], N.M. Sushchevskaya [a], E.P. Dubinin [c], D.V. Kuzmin [d]

[a] *Vernadsky Institute of Geochemistry and Analytical Chemistry, Russian Academy of Sciences, ul. Kosygina 19, Moscow, 119991, Russia*
[b] *Institut des Sciences de la Terre (ISTerre) Université J. Fourier-CNRS Maison des Goscience, Grenoble Alpes CS 40700 38058 GRENOBLE Cedex 9*
[c] *Moscow State University, Moscow, 119991, Russia*
[d] *V.S. Sobolev Institute of Geology and Mineralogy, Siberian Branch of the Russian Academy of Sciences, pr. Akademika Koptyuga 3, Novosibirsk, 630090, Russia*

Received 1 July 2016; accepted 8 February 2017
Available online xx October 2017

Abstract

Tholeiitic melts from the Bouvet triple junction (BTJ) of rift zones in the South Atlantic are moderately enriched rocks with specific lithophile-element patterns. The high (Gd/Yb)*N* values (up to 2.5) in some tholeiite compositions suggest the presence of garnet in the mantle source of primary BTJ melts. The high Ni and low Mn contents of most magnesian olivines determined by high-precision microprobe analysis suggest the presence of pyroxenite, along with typical peridotite, in the melting source. The unusually wide within-sample variation in the proportions of pyroxenitic component in the source region (X_{Px} Mn/Fe = 0–90%) indicates different degrees of mantle heterogeneity beneath the spreading zone. Based on geochemical data, this component is a silica-oversaturated eclogite, reacting with peridotite to form olivine-free pyroxenite in the melting source. His component is probably represented either by subducted and recycled oceanic crust or fragments of the ancient continental lithosphere buried into the mantle after Gondwana breakup. The observed global and local mantle heterogeneities might have been developed during a complex geodynamic evolution of the Southern Ocean, whose opening was affected by the activity of the Mesozoic Karoo-Maud plume and multiple jumps of the spreading axes, which led to the involvement of fragments of the early oceanic lithosphere in the melting process.

Keywords: Mid-Ocean Ridges; tholeiites; pyroxenitic component; peridotite; primary melts; Bouvet triple junction

Introduction

The opening of the South Atlantic Ocean during the Mesozoic was linked to the magmatic activity of the Parana-Etendeka plume. The effect of this igneous event on the development of oceanic crust was manifested in the formation of seamount groups and submarine rises, e.g., the major Walvis Ridge comprising the Rio Grande and Discovery Rises, and Shona Ridge. Plume activity has a direct influence of the geodynamic evolution of a spreading center along the Southern Mid-Atlantic Ridge (SMAR), which experienced a change in spreading direction during its evolution. The Bouvet triple junction (BTJ), located in the southernmost segment of the Mid-Atlantic Ridge and consisting of three seafloor structures, i.e., the Mid-Atlantic Ridge (MAR), American-Antarctic Ridge (AAR), and African-Antarctic Ridge (AfAR, also known in the western literature as the Southwest Indian Ridge, SWIR), is one the key geological features of the South Atlantic that records the main stages of the growth and reorganization of oceanic spreading zones. According to previous studies (Dickey et al., 1977; Douglass et al., 1995; LeRoex et al., 1982, 1983, 1985, 1992; Ligi et al., 1997, 1999; Peyve et al., 1995; Shilling et al., 1985; Simonov et al., 1996), the oceanic crust-forming process at the Bouvet triple junction was overprinted by plume magmatism related to Bouvet hotspot activity. These conditions were similar to the geotectonic setting of a number of seamounts and submarine rises north of the BTJ, in the Agulhas fault zone (e.g., Discovery, Shona).

It was found that three spreading ridges experienced a change in their configuration from ridge—ridge—ridge to the ridge—fault—fault during the evolution of the Atlantic Ocean shortly after Gondwana breakup (Dubinin et al., 1999; LeRoex et al., 1982). However, the regional tectonic setting and magmatic activity can be influenced by a change in the stress field as well as mantle dynamics of the BTJ segment. Bouvet

* Corresponding author.
E-mail address: nat-mig@yandex.ru (N.A. Migdisova)

Island was formed in this region approximately 2.0–2.5 million years ago (LeRoex et al., 1983). The present configuration of the BTJ appears to have remained stable for more than 1 Myr (Kleinrock and Morgan, 1988). The presence of a broad fault zone suggests that the BTJ was affected by ridge jumping and ridge overlapping (Ligi et al., 1997). The westernmost segment of the SWIR (Spiess Ridge) is a large volcanic structure trending SE–NW. The width of the ridge is 50 km; water depths at the foot of the ridge reach 1200–1400 m. The ridge is partially formed by a vast submarine caldera, 3.5–4.0 km in diameter, with flanks reaching about 320 m below sea level. The flanks of the ridge have a secondary crater, 1.0—2.5 km in diameter, reaching 800—900 m below sea level (Ligi et al., 1997). The Spiess Ridge shows a large axial positive magnetic anomaly. Unlike the Spiess Ridge, the SWIR segment located directly opposite Bouvet Island, is a typical slow-spreading ridge segment with a well-developed rift valley. Such a combination of different structures at the same location allows predictions of how geodynamics can influence ocean-floor topography and the character of regional magmatism.

The basalts from the western SWIR are moderately enriched tholeiites (Dickey et al., 1977; LeRoex et al., 1982, 1983, 1985, 1992; Peyve et al., 1995; Shilling et al., 1985; Simonov et al., Sushchevskaya et al., 1999; 1996, 2003).

This study utilizes new high-precision data on olivine and quench glass compositions to characterize magmatism and the nature of the enriched component in parental magmas from the Bouvet triple junction area. Our study aims to identify the main stages of the tectonic and magmatic evolution of the lithosphere of the Southern Ocean at the BTJ, using new and literature data.

Analytical methods

Locations of the dredges are shown in Fig. 1. Tholeiitic basalts were dredged during cruise S18 (dredge symbol S18) of the R/V Akademic Nikolai Strakhov and during cruise G96 of the R/V Gelendzhik-96 (G96). Rocks were dredged at 20 stations located on two main structures of the BTJ: directly opposite Bouvet Island (SWIR segment) and on the Spiess Ridge. The samples dredged are fragments of pillow lavas with well-preserved surficial quench features. Coordinates of the dredges are given in Table 1.

More than 500 olivine phenocrysts from tholeiitic basalts dredged from the BTJ area were analyzed by ion mass spectrometry on a CAMECA IMS3f microprobe at the Max Planck Institute for Chemistry (Mainz, Germany) using a 12.5 kV O^- primary ion beam, with a secondary voltage of 4.5 kV, an offset of –80 V, and a primary beam current $M/\Delta M$ = 300 nA. The energy slit was centered and opened to 25 V. San Carlos olivine standard was used for calibration

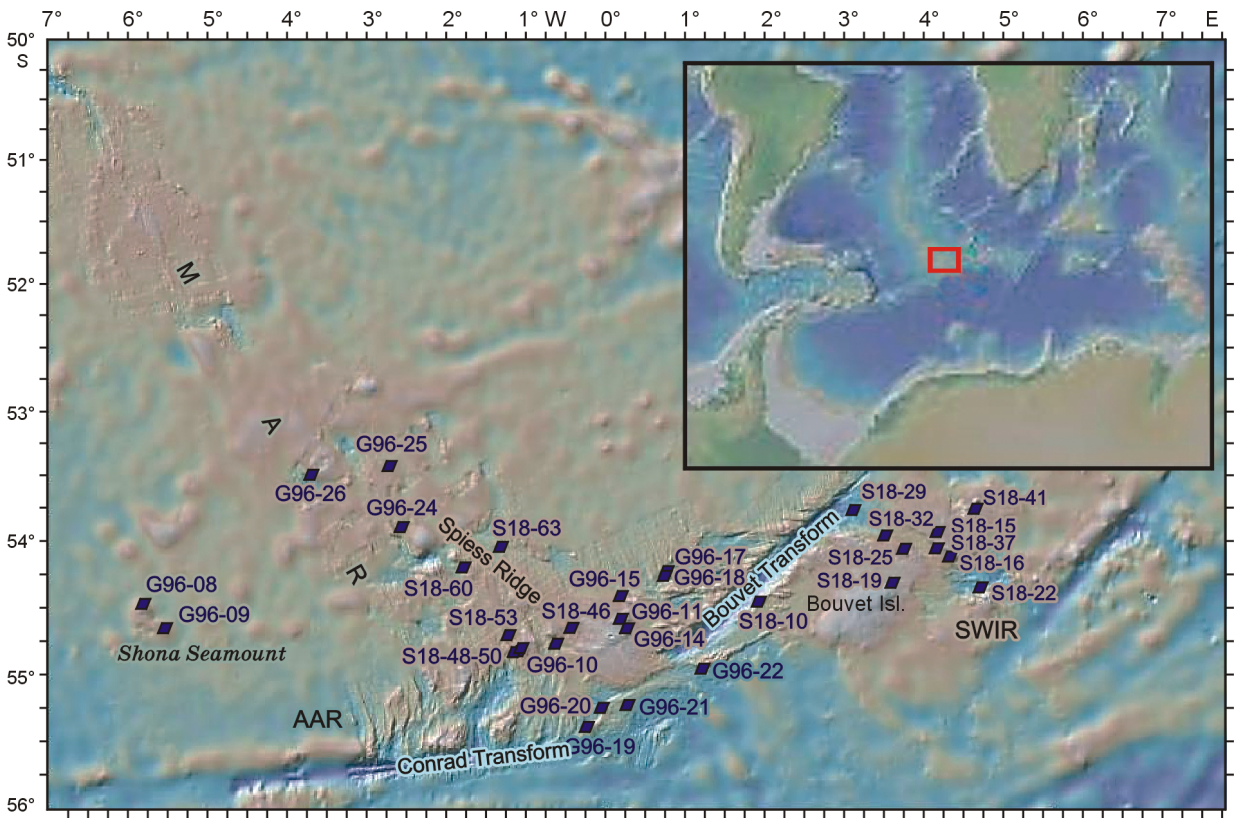

Fig. 1. Bathymetry map of the Bouvet triple junction area. Symbols indicate the location of stations dredged during cruise S18 of the R/V Akademik Strakhov and cruise G96 of the R/V Gelendzhik (G96) (Peyve et al., 1999).

Table 1. Major (wt.%) and trace (ppm) element composition of glasses from the Bouvet triple junction area

Component	TOR-1*	Spiess Ridge									
		G96-11/3	G96-12/17	G96-13/13	G96-15/1	G96-15/2	G96-15/3	G96-15/4	G96-15/7	G96-15/9	G96-15/25
		54.71° S	54.74° S	54.777° S	54.377° S	54.377° S	54.377° S	54.377° S	54.377° S	54.377° S	54.377° S
		0.053° W	0.07° E	0.073° E	0.039° W	0.039° W	0.039° W	0.039° W	0.039° W	0.039° W	0.039° W
		[d]600–400	600–400	1050	950–1060	950–1060	950–1060	950–1060	950–1060	950–1060	950–1060
SiO_2	49.26	50.62	56.04	50.80	50.97	50.60	51.53	50.73	50.65	50.60	50.69
TiO_2	0.60	2.51	2.34	2.50	2.40	2.60	2.75	2.57	2.63	2.48	2.53
Al_3O_3	15.10	14.41	13.75	14.26	14.41	14.40	14.17	14.24	14.00	14.32	14.27
FeO	7.56	12.04	12.06	12.07	11.89	12.01	12.71	11.82	12.59	11.89	11.86
MnO	0.20	0.20	0.24	0.19	0.20	0.19	0.19	0.18	0.19	0.19	0.20
MgO	13.08	4.97	2.64	4.82	5.04	5.03	4.82	4.97	4.93	4.94	5.17
CaO	12.38	9.66	6.10	9.37	9.88	9.67	9.52	9.73	9.39	9.83	9.75
Na_2O	1.61	3.76	3.88	3.78	3.73	3.81	2.55	3.74	3.73	3.65	3.71
K_2O	0.06	0.82	1.55	0.76	0.73	0.73	0.78	0.73	0.76	0.70	0.74
P_2O_5	0.01	0.44	0.69	0.44	0.38	0.34	0.38	0.32	0.33	0.33	0.36
S		0.11	0.08	0.15	0.13	0.14	0.15	0.14	0.14	0.13	0.14
Cl		0.07	0.30	0.11	0.06	0.06	0.07	0.07	0.06	0.06	0.06
Total	99.86	99.62	99.68	99.24	99.83	99.58	99.62	99.25	99.40	99.13	99.47
Mg#	75.7	42.4	28.1	41.6	43.1	42.8	40.3	42.8	41.1	42.6	43.7
K_2O/TiO_2	0.1	0.3	0.7	0.3	0.3	0.3	0.3	0.3	0.3	0.3	0.3
Ca		68,974	43,598	66,905	70,549	69,084	67,994	69,519	67,068	70,204	69,650
Rb		16.1	33.5	15.3	14.1	14.1	16.3	14.6	15.6	14.5	14.2
Ba		180	285	173	160	158	175	160	167	162	159
Th		2.2	4.9	2.2	2.0	2.1	2.2	2.0	2.1	2.0	2.1
U		0.65	1.51	0.63	0.58	0.58	0.63	0.59	0.60	0.59	0.58
Nb		27.9	46.3	27.6	25.0	24.6	27.5	24.8	26.0	25.0	24.7
Ta		1.7	2.7	1.7	1.5	1.5	1.6	1.5	1.6	1.5	1.5
La		21.2	38.8	20.6	19.2	19.0	21.3	19.3	20.0	19.5	19.0
Ce		46.1	84.3	45.4	42.7	42.2	46.8	42.5	44.0	42.9	42.1
Pb		1.6	3.0	1.5	1.5	1.5	1.6	1.5	1.6	1.5	1.5
Pr		6.2	11.2	6.1	5.8	5.7	6.3	5.7	5.9	5.8	5.7
Nd		28.8	50.2	28.0	26.7	26.6	29.1	26.5	27.4	27.0	26.3
Sr		287	184	257	267	259	261	258	259	267	259
Sm		7.3	12.3	7.2	6.9	6.7	7.4	6.7	7.0	6.9	6.7
Zr		225	472	219	211	208	228	209	220	213	206
Hf		5.3	11.1	5.4	5.1	5.2	5.5	5.0	5.1	5.2	5.1
Eu		2.4	3.5	2.4	2.3	2.3	2.5	2.3	2.4	2.3	2.3
Ti		15,607	13,545	15,020	14,704	14,591	16,142	14,485	15,419	14,710	14,596
Gd		8.1	13.5	8.1	7.7	7.7	8.2	7.6	7.8	7.8	7.6
Tb		1.3	2.2	1.3	1.2	1.2	1.3	1.2	1.2	1.2	1.2
Dy		7.7	13.6	7.8	7.5	7.4	7.9	7.3	7.6	7.5	7.3
Ho		1.5	2.7	1.5	1.5	1.5	1.6	1.4	1.5	1.5	1.5
Y		38.5	71.6	38.6	37.0	36.8	40.2	36.5	38.2	37.4	36.3
Er		4.0	7.6	4.1	3.9	3.9	4.2	3.9	4.0	3.9	3.9
Tm		0.54	1.09	0.55	0.54	0.54	0.58	0.53	0.55	0.55	0.53
Yb		3.6	7.4	3.7	3.6	3.7	4.0	3.6	3.7	3.7	3.6
Lu		0.52	1.06	0.54	0.53	0.53	0.57	0.52	0.54	0.53	0.52
Ni		32.1	1.3	23.2	24.8	21.9	20.4	25.4	21.7	24.7	24.6
Cu		69.4	31.8	53.1	63.4	56.7	69.3	61.4	54.7	63.9	48.1
Zn		119	155	128	121	124	144	121	126	125	124
Mn		1571	1773	1558	1551	1549	1693	1580	1670	1559	1557
Sc		36.2	23.7	36.1	37.1	36.0	36.3	36.6	36.4	36.7	36.6
Co		39.4	23.1	38.4	40.1	39.7	41.8	40.5	41.4	40.6	40.0
Li		7.2	14.3	7.1	6.8	6.8	7.2	7.1	7.8	6.9	7.8
V		283	136	281	284	282	300	282	292	285	285
Pd		0.20	0.49	0.21	0.20	0.18	0.25	0.20	0.20	0.21	0.22
W		0.27	0.59	0.27	0.25	0.27	0.27	0.26	0.25	0.27	0.27
Fe		93,687	92,645	92,913	92,388	91,735	100,077	93,571	98,498	93,612	91,984
Fe/Mn		59.6	52.3	59.7	59.6	59.2	59.1	59.2	59.0	60.0	59.1
Zn/Mn		0.08	0.09	0.08	0.08	0.08	0.08	0.08	0.08	0.08	0.08
Zn/Fe·10		12.7	16.7	13.8	13.1	13.5	14.3	12.9	12.8	13.4	13.5
La/Sm		2.9	3.2	2.9	2.8	2.8	2.9	2.9	2.9	2.8	2.8
Nb/U		43.1	30.5	43.9	43.4	42.5	43.9	42.4	43.3	42.4	42.3
Dy/Yb		2.1	1.8	2.1	2.1	2.0	2.0	2.0	2.0	2.0	2.0

(*continued on next page*)

Table 1 (*continued*)

Component	SWIR segment												
	S18-15/2 54.05° S 4.37° E [d]1480	S18-16/6 54.9° S 3.90° E 2000	S18-16/42 54.9° S 3.90° E 2000	S18-19/4 54.20° S 3.53° E 1600	S18-22/21 54.21° S 4.41° E 2200	S18-22/22 54.21° S 4.41° E 2200	S18-29/1 53.80° S 3.60° E 2400	S18-29/2 53.80° S 3.60° E 2400	S18-29/3 53.80° S 3.60° E 2400	S18-29/4 53.80° S 3.60° E 2400	S18-29/5 53.80° S 3.60° E 2400	S18-29/10 53.80° S 3.60° E 2400	S18-29/12 53.80° S 3.60° E 2400
SiO_2	49.44	51.64	51.69	59.00	50.29	50.29	49.88	49.67	49.86	51.28	49.92	49.86	50.09
TiO_2	2.82	2.42	2.49	1.53	2.47	2.48	2.50	2.41	2.39	1.85	2.31	2.38	1.92
Al_3O_3	14.82	14.53	14.53	14.86	14.86	14.91	15.85	15.77	15.80	16.01	16.04	15.79	15.85
FeO	10.84	11.31	11.54	9.51	10.29	10.23	9.15	9.14	9.30	9.30	9.03	9.17	8.65
MnO	0.20	0.22	0.20	0.23	0.16	0.17	0.15	0.14	0.14	0.17	0.14	0.14	0.14
MgO	5.80	5.09	4.74	1.50	5.76	5.77	6.91	6.96	6.99	7.10	6.68	6.98	6.97
CaO	10.56	9.46	9.27	4.43	10.72	10.73	10.36	10.34	10.35	11.44	10.62	10.31	11.80
Na_2O	3.32	3.51	3.68	5.12	3.28	3.30	3.22	3.27	3.22	1.98	3.05	3.29	3.00
K_2O	0.81	0.77	0.85	2.88	0.75	0.79	1.02	1.05	1.04	0.58	1.02	1.03	0.72
P_2O_5	0.55	0.33	0.35	0.55	0.41	0.40	0.36	0.34	0.43	0.23	0.33	0.36	0.25
S	0.13	0.11	0.12	0.02	0.13	0.13	0.08	0.09	0.10	0.09	0.09	0.09	0.09
Cl	0.03	0.03	0.03	0.12	0.04	0.03	0.03	0.03	0.03	0.03	0.03	0.03	0.03
Total	99.30	99.41	99.50	99.75	99.23	99.16	99.51	99.22	99.64	100.06	99.26	99.42	99.51
Mg#	48.8	44.5	42.3	21.9	49.9	50.1	57.4	57.6	57.3	57.7	56.9	57.5	58.9
K_2O/TiO_2	0.3	0.3	0.3	1.9	0.3	0.3	0.4	0.4	0.4	0.3	0.4	0.4	0.4
Ca	75,395	67,561	66,199	31,655	76,582	76,644	74,023	73,832	73,909	81,723	75,857	73,671	84,319
Rb	15.1	14.2	16.1	54.5	14.4	14.4	19.0	19.3	19.1	11.1	18.6	19.0	13.9
Ba	171	153	162	539	163	172	228	224	224	104	220	222	145
Th	2.0	1.8	2.1	7.9	1.9	1.9	2.0	2.0	2.0	1.6	1.9	2.0	1.7
U	0.59	0.52	0.55	2.38	0.54	0.57	0.54	0.56	0.57	0.45	0.54	0.57	0.47
Nb	26.8	21.6	23.2	96.5	24.1	24.8	28.6	28.3	28.2	18.9	27.2	28.0	21.6
Ta	1.7	1.4	1.5	5.6	1.6	1.5	1.8	1.8	1.7	1.2	1.7	1.7	1.3
La	20.0	18.3	20.2	66.1	19.2	19.6	22.3	21.0	21.0	13.7	20.5	20.9	15.6
Ce	44.3	37.5	39.8	128.3	40.6	41.4	44.0	44.6	44.4	30.2	43.0	44.2	33.7
Pb	1.5	1.5	1.7	4.6	1.4	1.5	1.5	1.8	1.7	1.2	1.7	1.7	1.3
Pr	6.0	5.0	5.4	14.9	5.3	5.2	5.4	5.8	5.7	4.0	5.6	5.8	4.4
Nd	28.0	23.8	26.6	65.3	24.4	24.5	24.6	25.9	25.6	18.3	25.1	25.8	19.8
Sr	307	231	239	279	283	287	418	400	399	208	399	399	277
Sm	6.7	6.0	6.9	14.5	6.0	6.1	5.9	6.1	5.9	4.7	5.9	6.0	4.7
Zr	185	205	247	615	188	180	184	194	192	138	188	193	150
Hf	4.5	4.8	5.9	13.1	4.4	4.1	4.4	4.6	4.5	3.4	4.4	4.6	3.6
Eu	2.4	2.1	2.3	4.4	2.2	2.3	2.1	2.0	2.0	1.6	2.0	2.0	1.6
Ti	16,278	14,646	15,210	9606	15,561	16,363	15,131	13,724	13,651	10,394	13,520	13,595	10,680
Gd	7.3	6.6	7.5	13.2	6.5	5.8	5.7	6.1	6.2	5.3	5.9	6.1	5.2
Tb	1.1	1.1	1.2	2.0	1.0	0.9	0.9	0.9	0.9	0.9	0.9	0.9	0.8
Dy	6.5	8.0	9.1	14.3	7.5	6.7	5.7	5.4	5.5	5.6	5.3	5.4	5.1
Ho	1.3	1.7	1.9	2.7	1.4	1.4	1.1	1.0	1.0	1.1	1.0	1.0	1.0
Y	31.7	37.6	46.8	61.9	31.6	29.5	22.9	26.3	26.1	28.8	25.8	26.2	25.8
Er	3.4	4.1	4.7	6.4	3.5	3.1	2.6	2.7	2.7	3.1	2.6	2.7	2.7
Tm	0.45	0.53	0.59	0.85	0.46	0.41	0.36	0.36	0.37	0.44	0.35	0.37	0.38
Yb	3.0	3.9	4.6	6.2	3.2	3.0	2.5	2.5	2.4	3.0	2.4	2.4	2.6
Lu	0.43	0.58	0.65	0.89	0.45	0.44	0.32	0.34	0.35	0.45	0.34	0.35	0.37
Ni	43.6	26.0	21.8	1.5	37.1	39.9	104.3	109.9	104.9	84.0	96.3	107.7	87.1
Cu	40.6	32.2	31.7	5.1	43.4	42.2	40.2	40.1	39.6	39.2	41.5	39.7	48.3
Zn	112	106	91	184	93	107	88	94	96	89	90	96	85
Mn	1466	1421	1442	1533	1368	1344	1110	1185	1155	1315	1179	1181	1253
Sc	38.0	38.7	42.8	17.0	37.3	35.5	30.4	30.6	30.6	39.4	30.7	30.6	38.2
Co	36.7	36.6	34.1	8.2	36.7	37.2	38.2	39.1	38.4	37.3	37.4	38.9	41.0
Li	6.0	8.0	9.0	15.2	6.7	6.8	6.6	5.9	5.8	11.8	5.9	5.9	5.3
V	322	317	307	14	289	306	238	243	240	280	241	240	257
Pd	0.21	nd	nd	nd	nd	nd	nd	0.19	0.18	0.14	0.19	0.20	0.13
W	0.30	0.28	0.30	1.19	0.30	0.26	0.31	0.29	0.29	0.21	0.29	0.28	0.25
Fe	83,706	88,099	86,092	72,686	83,744	80,951	70,757	71,994	71,561	71,673	70,350	71,924	70,877
Fe/Mn	57.1	62.0	59.7	47.4	61.2	60.2	63.8	60.7	61.9	54.5	59.7	60.9	56.5
Zn/Mn	0.08	0.07	0.06	0.12	0.07	0.08	0.08	0.08	0.08	0.07	0.08	0.08	0.07
Zn/Fe·10	13.4	12.0	10.6	25.3	11.0	13.2	12.4	13.1	13.4	12.4	12.7	13.3	12.1
La/Sm	3.0	3.0	2.9	4.5	3.2	3.2	3.8	3.5	3.5	2.9	3.5	3.5	3.3
Nb/U	45.6	41.2	42.1	40.6	44.5	43.4	53.5	50.2	49.3	42.3	50.5	49.5	45.7
Dy/Yb	2.2	2.0	2.0	2.3	2.4	2.2	2.3	2.2	2.2	1.8	2.2	2.2	2.0

(*continued on next page*)

Table 1 (*continued*)

Component	SWIR segment												
	S18-29/15 53.80° S 3.60° E [d]2400	S18-32/9 53.89° S 3.45° E 2600	S18-37/1 54.12° S 3.83° E 1380	S18-37/2 54.12° S 3.83° E 1380	S18-37/3 54.12° S 3.83° E 1380	S18-37/4 54.12° S 3.83° E 1380	S18-37/5 54.12° S 3.83° E 1380	S18-37/6 54.12° S 3.83° E 1380	S18-37/7 54.12° S 3.83° E 1380	S18-37/8 54.12° S 3.83° E 1380	S18-37/9 54.12° S 3.83° E 1380	S18-37/10 54.12° S 3.83° E 1380	S18-37/11 54.12° S 3.83° E 1380
SiO_2	50.48	50.39	51.52	50.95	50.82	50.91	50.81	51.27	50.91	51.50	50.94	51.23	49.65
TiO_2	1.95	1.37	3.11	3.44	3.33	3.04	3.39	3.29	3.34	3.15	3.20	3.42	3.03
Al_3O_3	15.66	15.63	14.47	13.93	14.03	14.09	14.06	14.36	14.13	14.35	14.18	14.37	14.81
FeO	8.93	9.72	12.81	12.74	12.86	12.70	12.69	12.94	12.78	13.01	12.94	12.92	11.06
MnO	0.16	0.19	0.22	0.20	0.22	0.21	0.21	0.23	0.23	0.21	0.20	0.21	0.19
MgO	6.86	7.85	4.42	4.14	4.31	4.32	4.31	4.29	4.32	4.34	4.23	4.36	5.29
CaO	11.46	11.87	8.83	8.69	8.67	8.62	8.65	8.73	8.64	8.80	8.60	8.75	10.11
Na2O	3.08	2.89	2.67	3.51	3.72	3.73	3.64	3.16	3.77	2.54	3.74	3.17	3.30
K2O	0.61	0.12	1.08	1.18	1.10	1.11	1.09	1.12	1.07	1.06	1.10	1.09	1.00
P_2O_5	0.26	0.09	0.47	0.46	0.46	0.52	0.47	0.55	0.45	0.47	0.44	0.47	0.55
S	0.08	0.11	0.15	0.14	0.14	0.14	0.12	0.15	0.12	0.14	0.13	0.14	0.13
Cl	0.02	0.01	0.10	0.09	0.09	0.10	0.09	0.11	0.10	0.10	0.09	0.10	0.05
Total	99.55	100.23	99.84	99.47	99.75	99.48	99.52	100.19	99.84	99.69	99.79	100.24	99.18
Mg#	57.8	59.0	38.1	36.7	37.4	37.8	37.7	37.1	37.6	37.3	36.8	37.6	46.0
K_2O/TiO_2	0.3	0.1	0.3	0.3	0.3	0.4	0.3	0.3	0.3	0.3	0.3	0.3	0.3
Ca	81,846	84,786	63,074	62,102	61,929	61,577	61,759	62,374	61,712	62,839	61,419	62,509	72,189
Rb	12.6	1.9	20.7	21.9	20.5	20.6	20.4	21.5	20.3	20.6	20.7	20.7	19.4
Ba	126	23	209	220	207	209	206	212	205	205	208	207	198
Th	1.6	0.2	2.9	3.0	2.9	2.9	2.9	2.8	2.9	2.9	2.8	2.9	2.6
U	0.47	0.06	0.86	0.89	0.85	0.87	0.85	0.86	0.85	0.85	0.86	0.85	0.81
Nb	21.5	2.7	37.4	39.7	37.3	37.8	37.1	37.9	37.0	37.0	37.5	37.2	35.5
Ta	1.3	0.2	2.4	2.5	2.4	2.4	2.4	2.3	2.3	2.3	2.3	2.3	2.2
La	14.9	3.4	26.5	27.7	26.2	26.6	26.3	26.4	26.0	26.4	26.2	26.4	24.7
Ce	32.5	9.7	57.9	60.4	57.7	58.3	57.4	57.8	56.9	57.3	58.1	57.6	52.8
Pb	1.3	0.6	2.1	2.1	2.1	2.1	2.0	2.2	2.1	2.1	2.1	2.1	1.9
Pr	4.3	1.6	7.8	8.1	7.7	7.8	7.7	7.7	7.6	7.7	7.7	7.7	7.0
Nd	19.9	9.0	35.1	36.3	34.6	35.3	34.7	34.5	34.4	34.7	34.9	34.9	31.5
Sr	227	122	278	281	276	276	275	279	272	276	274	278	355
Sm	5.0	3.1	8.3	8.7	8.3	8.5	8.5	8.4	8.3	8.4	8.4	8.4	7.4
Zr	152	77	277	286	271	274	272	276	271	273	276	275	239
Hf	3.7	2.0	6.7	7.0	6.6	6.8	6.7	6.4	6.6	6.7	6.6	6.6	5.5
Eu	1.7	1.2	2.7	2.8	2.7	2.8	2.7	2.7	2.7	2.7	2.7	2.7	2.5
Ti	10,797	7375	20,139	2,0425	19,727	19,675	19,798	19,915	19,669	20,100	19,691	19,878	17,675
Gd	5.7	4.3	9.1	9.4	9.0	9.2	9.1	9.0	8.9	9.1	9.0	9.1	7.5
Tb	0.9	0.7	1.4	1.5	1.4	1.4	1.4	1.4	1.4	1.4	1.4	1.4	1.1
Dy	5.9	4.9	8.6	8.8	8.5	8.7	8.6	8.7	8.5	8.6	8.5	8.7	6.7
Ho	1.2	1.0	1.7	1.7	1.7	1.7	1.7	1.7	1.7	1.7	1.7	1.7	1.3
Y	29.7	27.0	43.2	43.4	42.5	43.1	42.7	42.5	42.5	43.0	42.4	43.2	32.5
Er	3.2	2.9	4.6	4.6	4.5	4.6	4.6	4.5	4.5	4.6	4.5	4.6	3.3
Tm	0.44	0.42	0.63	0.64	0.62	0.64	0.63	0.62	0.62	0.62	0.62	0.64	0.45
Yb	3.0	2.9	4.3	4.3	4.3	4.3	4.3	4.3	4.2	4.2	4.2	4.3	3.1
Lu	0.44	0.43	0.63	0.62	0.62	0.63	0.62	0.61	0.61	0.62	0.60	0.63	0.42
Ni	76.5	110.3	16.1	13.3	15.0	14.9	16.0	16.9	15.6	15.9	15.0	16.5	34.6
Cu	50.9	70.5	26.4	29.4	26.2	25.9	26.1	25.8	26.1	26.3	25.9	25.7	34.1
Zn	85	86	136	137	134	130	136	129	133	137	136	127	105
Mn	1254	1394	1698	1669	1663	1648	1680	1712	1667	1688	1667	1705	1460
Sc	38.5	43.8	36.0	34.9	35.0	35.0	35.4	35.2	35.2	36.0	35.0	35.6	34.6
Co	35.9	43.8	38.5	37.4	37.8	37.6	38.5	39.0	37.6	38.3	38.1	38.2	36.8
Li	5.7	5.7	8.1	8.1	8.0	8.2	8.0	8.3	7.9	7.9	8.0	8.1	6.5
V	269	278	381	374	375	374	379	382	376	383	374	381	320
Pd	0.14	0.08	0.26	0.29	0.25	0.27	0.30	0.23	0.29	0.24	0.26	0.25	0.20
W	0.24	0.02	0.38	0.42	0.39	0.41	0.39	0.42	0.39	0.41	0.40	0.38	0.39
Fe	69,552	76,959	101,290	99,670	99,399	98,564	100,894	102,489	98,989	100,449	99,564	101,047	85,667
Fe/Mn	55.5	55.2	59.7	59.7	59.8	59.8	60.0	59.9	59.4	59.5	59.7	59.2	58.7
Zn/Mn	0.07	0.06	0.08	0.08	0.08	0.08	0.08	0.08	0.08	0.08	0.08	0.07	0.07
Zn/Fe·10	12.3	11.2	13.4	13.7	13.4	13.2	13.5	12.5	13.4	13.6	13.6	12.6	12.2
La/Sm	3.0	1.1	3.2	3.2	3.1	3.1	3.1	3.1	3.1	3.1	3.1	3.2	3.3
Nb/U	45.3	44.2	43.6	44.6	43.8	43.4	43.4	44.1	43.3	43.5	43.8	44.0	44.1
Dy/Yb	1.9	1.7	2.0	2.1	2.0	2.0	2.0	2.0	2.0	2.0	2.0	2.0	2.2

Note. TOR-1* is a modified quench glass composition relative to the initial composition of TOR-1 (Sushchevskaya et al., 1999). Analyses were performed at the Max Planck Institute (Mainz, Germany) by ion mass spectrometry on a CAMECA IMS3f microprobe (analyst D. Kuzmin). [d]Depth (m).

and accuracy assessment of measurements (Jarosevich et al., 1980). All measurements of Si, Fe, Mn, Ni, Ca, and Al were corrected for deviation of San Carlos standard from the reference values. For trace elements, the measurement conditions give detection limits of 6–15 ppm based on 3-sigma criterion by JEOL software, and errors of 15–30 ppm for trace elements and 0.01 mol.% for Fo content relative to olivine standard established by measurements on olivine standard. Each trace element analysis consisted of 5 scans, starting from ^{16}I mass (for magnet adjustment), then over the sequence ^{30}Si, ^{39}K, ^{44}Ca, ^{47}Ti, ^{51}V, ^{52}Cr, ^{88}Sr, ^{89}Y, ^{90}Zr, and ^{93}Nb, each mass for elements from 133 to 180. Oxide interferences, for example, light rare-earth element (LREE) oxides interfering with and heavy rare earth elements (HREE), were corrected using peak deconvolution, following the procedure proposed by Zinne and Crozaz (1986) and Fahey et al. (1987). Relative sensitivity factors (RSF defined as the ratio of total ionic intensity for a given element to the ionic intensity of Si divided by the respective element ratios in atomic concentration for the material, i.e., $(K^+/Si^+)/(K/Si)$) were defined based on the analyses of reference basaltic glasses (Jochum et al., 2000). Instrument drift was controlled and necessary correction applied

based on daily replicate analyses of KL2-G reference glass (Jochum et al., 2000). Estimated analytical error was better than 20% (2σ RSE) for all elements, except Gd, for which the error was between 18 and 25% (Gurenko and Sobolev, 2006; Gurenko et al., 2009).

Magma composition

The analysis of more than 300 samples of quench glasses collected at 20 stations revealed a wide major element variation in melts from the Bouvet triple junction. The two large structures (Spiess Ridge and SWIR segment) generally show similar variations in terms of major element composition of basalt quench glasses (Sushchevskaya et al., 2003). Almost all major elements demonstrated a good correlation with Mg contents of glasses. Toward more evolved compositions, samples show a significant decrease in CaO and Al_2O_3 and an increase in FeO, Na_2O, K_2O, and TiO_2 with decreasing MgO contents (from 8 to 1 wt.%), with (Fig. 2). The observed trends were derived from crystallization differentiation. Comparisons of the compositions of the BTJ quench glasses with the available data on the South Atlantic (MAR 50º–54º S) (LeRoex et al., 1998) and the database at http://petdb.org/ show that compositional fields for the BTJ glasses are much broader than those for the SMAR typical oceanic tholeiites. The SiO_2 range is 49.5–59 wt.%. FeO and TiO_2 increase with decreasing MgO, reaching 13 and 3.7 wt.%, respectively. However, at 3 wt.% MgO, probably due to the appearance of titanomagnetite, the contents of FeO and TiO_2 decrease significantly at the end of differentiation to 9.0 and 1.5 wt.%, respectively. The K_2O content of the BTJ melt is unusually high compared with typical rift-derived tholeiites; it varies from 0.1 to 1.6 wt.% in glasses from the Spiess Ridge and from 0.1 to 2.9 wt.% in glasses from the SWIR segment. The K_2O/TiO_2 ratio used as an indicator of source enrichment is highly heterogeneous in the BTJ glasses because it is relatively insensitive to the effects of crystallization processes in occurring in the magmatic system (Fig. 2). Based on this parameter, we can infer that both depleted rift-derived melts and enriched melts are present in the BTJ area. The most enriched tholeiites were dredged from the slopes of Bouvet Island. Interestingly, both enriched and depleted quench glasses were dredged at several stations in the northern segment of the SWIR. The presence of a group of quench glasses with low Na_2O (<2.5 wt.%) provides evidence for mantle heterogeneity beneath the BTJ.

The evolution of the BTJ magmatic system took place through the classic process of crystallization differentiation of tholeiitic melts: $Ol \rightarrow Ol + Pl \rightarrow Ol + Pl + Cpx \pm Mgt$ (Sushchevskaya et al., 1999; Migdisova et al., 2004). Calculations using the Petrolog software (Danyushevsky and Plechov, 2011) show that the main group of quench glasses form a cluster along an olivine-plagioclase cotectic. Natural phenocrysts were not in equilibrium with quench glasses and represent low-temperature crystallization products of magma evolution processes. It is possible that they formed by mixing of melts during eruption on the sea floor or in an intermediate magma chamber (Sushchevskaya et al., 2003; Migdisova et al., 2004).

The compositions of BTJ parental melts are close to those of melts formed during the experiments on partial melting of MPY pyrolite (Falloon and Green, 1987; Falloon et al., 1988) at $T = 1348$ ℃, $P = 15$ kbar and degrees of melting of 15–20%. At the same time, these melts are geochemically similar to TOR-1 type primary melts[1] (Table 1), which were earlier proposed as a representative parental melt for the Bouvet magmas (Sushchevskaya et al., 1999). At the same time, the BTJ primary melts differ from a typical parent tholeiitic magma by a high water content. The primary melts are inferred to have approximately 0.2 wt.% H_2O.

The parameters of crystallization of BTJ basalts calculated using the Petrolog software (Danyushevsky and Plechov, 2011) indicate that they crystallized at pressures between 2 and 5 kbar and temperatures of 1100–1300 ℃ (Fig. 3*a*). This is consistent with the results of Nimis and Ulmer (1998) who employed an approach based on the dependence of crystallizing clinopyroxene on pressure and temperature (Fig. 3*b*) (Migdisova et al., 2004). These crystallization conditions can be realized in an intermediate magma chamber beneath the ridge.

Composition of olivine phenocrysts

The analyzed compositions of olivine (more than 300 crysts were analyzed), the main liquidus phase of tholeiitic melts,

[1] https://www.researchgate.net/publication/315475743_Data_on_olivine_phenocrysts_from_tholeiitic_melts_dredged_in_the_Bouvet_Triple_Junction_region

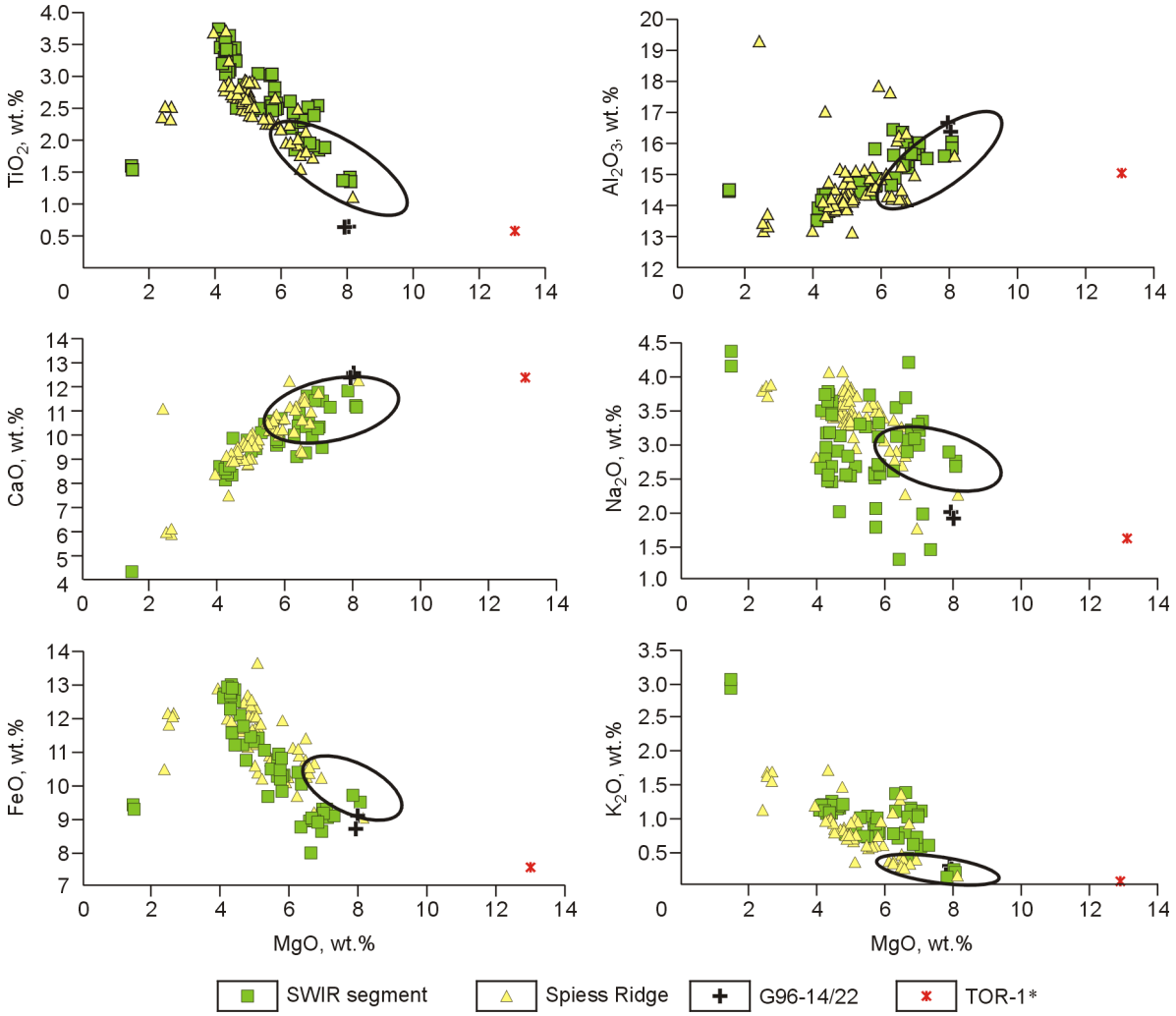

Fig. 2. Major element variation diagrams for quench glasses from BTJ basalts. MORB field for southern segment of the MAR at 40°–56° S is from LeRoex et al. (1982) and database at http://petdb.org/.

show that olivine phenocrysts are highly heterogeneous in terms of their Fo content as well as Cà, Ni, Mn, and Cr. Olivine composition varies from Fo_{72} to Fo_{92}. The most magnesian olivine (Fo_{91}) was recovered from the SWIR area (Table 1)[1].

Trace element concentrations (ppm) range from 120 to 240 for Co, from 360 to 3000 for Ni, from 1100 to 3000 for Mn, from 5 to 2500 for Ca, and from 14 to 700 for Cr. The observed variations significantly exceed the obtained 2σ SD analytical errors (± 0.01 for Fo, ± 70–80 ppm for Ca and Ni, and ± 40 ppm for Mn and Cr). The scatter in trace element concentrations and variations in Mg# of olivine reflect crystallization differentiation processes in the magma chamber. The Cr and Ni contents show a positive correlation with each other and their concentrations decrease with decreasing Fo content (Fig. 4). Mn exhibits a negative correlation with Fo. It is noteworthy that the above elements (Ni, Cr, Mn) vary in a narrow range at any Mg# of olivine. Contents of these elements are highly variable in the olivine phenocrysts from each sample dredged from the BTJ area. For example, one olivine phenocryst (Fo_{86}) has NiO ranging from 0.1 to 0.3 wt.%. Such compositional heterogeneity may be due to the presence of different parental melts in the Bouvet area.

There is no strong correlation between Ca and Fo. Most olivine phenocrysts contain about 2000 ppm Ca, which typical of olivines from basalt magmas (Fig. 4). The compositions of olivine phenocrysts from sample G96-14/22 define a separate compositional group with lower Ca concentrations. The lowest Ca concentrations (1200 ppm) are observed in the phenocrysts from sample S18-60/1 recovered from the MAR segment near the BTJ area (Kamenetsky et al., 2001). The Ca concentrations below 2000 ppm in olivine with a composition around Fo_{87-90} indicate the involvement of a pyroxenitic component in the melting of a peridotite source of BTJ magmas (Herzberg, 2006; Sobolev et al., 2007).

Concentrations of Cr exhibit positive correlations with Mg# of olivine. Olivine phenocrysts with Fo_{90-91} compositions have the highest Cr values (500—600 ppm), which are typical of MORB olivines. Since the Cr values of melts largely depend on the presence of garnet and/or spinel in a peridotite source (Sobolev et al., 2007), the source of the BTJ basalts is likely to have variable concentrations of spinel and garnet.

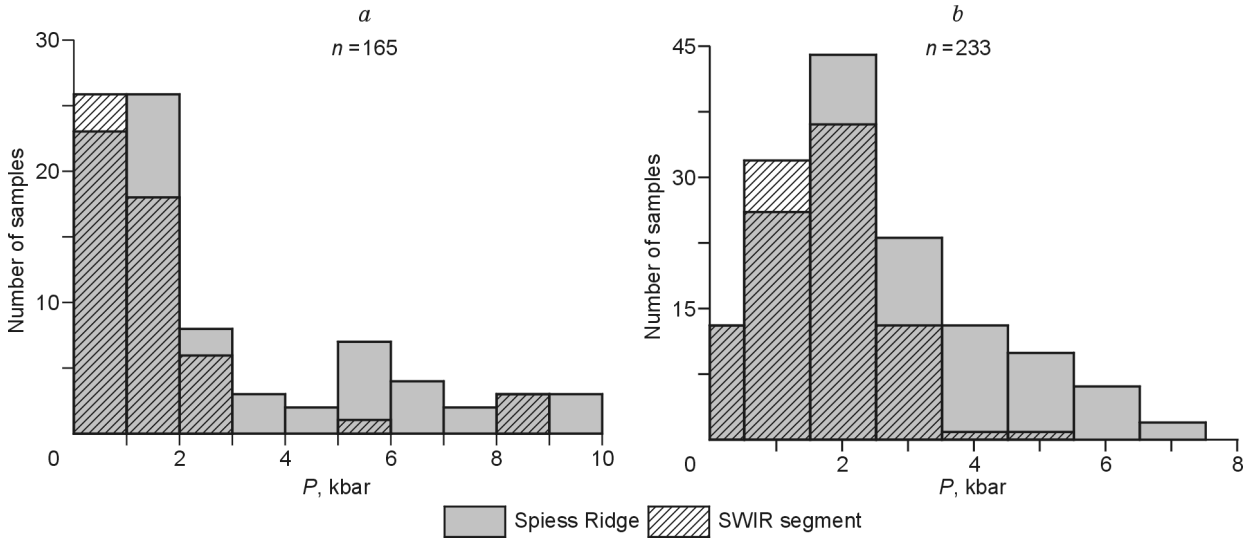

Fig. 3. Estimated pressures of magma crystallization beneath Bouvet segment. Most samples have pressures of 0–3 kbar, which suggests crystallization under near-surface conditions. The second peak at P = 5–7 kbar marks crystallization in the intermediate magma chamber beneath the ridge. *a*, Pressures calculated using the Petrolog model (Danyushevsky and Plechov, 2011). The Petrolog software offers an algorithm that allows modeling fractional and equilibrium crystallization, and reverse crystallization differentiation at variable pressure, melt oxidation state and melt H_2O content. Crystallization modeling is based on the principle of pseudoliquidus temperatures (Danyushevsky and Plechov, 2011). *b,* Pressures calculated at temperatures of 1100–1150 °C using the method of Nimis and Ulmer (1998).

The variation diagrams (Fig. 4) include the fields for olivines from the BTJ basalts, tholeiites from the Sequeiros fault zone (Pacific Ocean) (Goss et al., 2010) and SMAR at 50º–56° S, reflecting compositional variations in typical oceanic ridge tholeiites, as well as olivines from Hawaiian Mauna Loa volcano, a deep-seated hotspot (Sobolev et al., 2007) and data from the database (http://petdb.org/). As can be seen, olivine phenocrysts from the BTJ tholeiites show much more variable compositions than olivines from the Sequeiros fault zone (more than 100 analyses) and SMAR (more than 290 analyses). Although olivines in Mauna Loa basalts exhibit a broader range of Mn, Ca, Ni, and Cr contents, mainly due to the higher alkalinity of melts and rather undifferentiated magmas (Fo_{90-82}), the BTJ olivines overlap the field of Mauna Loa olivines. These magmatic systems were selected for comparison with the BTJ area because of the availability of data on these "classic" geochemical and petrological objects for study. Therefore, the above data on the compositions of olivine phenocrysts from the BTJ area (e.g., their Ni and Mn contents) suggest the presence of multiple populations of phenocrysts and olivines derived from potentially different parental melts.

Reconstruction of the composition of the parental magmas for BTJ tholeiites from olivine phenocryst data

The source composition of tholeiitic melts from the BTJ area was estimated using the method by Sobolev et al. (2005, 2007), which considers the compositions of olivine phenocrysts in magmatic systems and relationships between Ni and Mn under different conditions of magma generation. The combination of high Ni and low Mn contents of olivine is usually inherited from the parental melt, which is a mixture of peridotitic and pyroxenitic components. The major and trace element compositions of magmas produced by melting of a peridotite source having an olivine + orthopyroxene + clinopyroxene ± garnet ± spinel composition are typical of the depleted tholeiites, which is subsequently reflected in the composition of crystallizing phenocrysts. At the same time, melting of an olivine-free pyroxenite (orthopyroxene + clinopyroxene ± garnet ± spinel) produces melts, which are unusually enriched in Si and Ni and depleted in Mg, Ca, and Mn. Mixing of peridotite and pyroxenite source materials ultimately produces hybrid magmas. Olivines crystallized from such magmas would also be expected to have high Ni and low Mn and Ca contents.

Olivine is the dominant phase in the rocks that formed by melting of a peridotite source, while clinopyroxene is the main mineral phase of the melts derived from a pyroxenite source. These two minerals acting as concentrators of different chemical elements define the ultimate composition of the produced melts. The relative proportions of pyroxenitic component in a primary source can be determined from Ni and Mn contents of olivine phenocrysts derived from hybrid melts.

Using the method described in Sobolev et al. (2005, 2007), we calculated the Ni/(Mg/Fe)/1000, Ca/Fe, 100Mn/Fe parameters for the compositions of olivine phenocrysts used in this study. Trace element concentrations in olivine normalized to its Fe and Mg/Fe values were used to estimate the concentrations of these elements in olivines with similar Fe and Mg/Fe values. This allowed us to ignore the effects of melt differentiation and obtain the compositions reflecting the actual variation in Ni and Mn contents of the melt. The values of these parameters for olivine phenocrysts from the BTJ tholei-

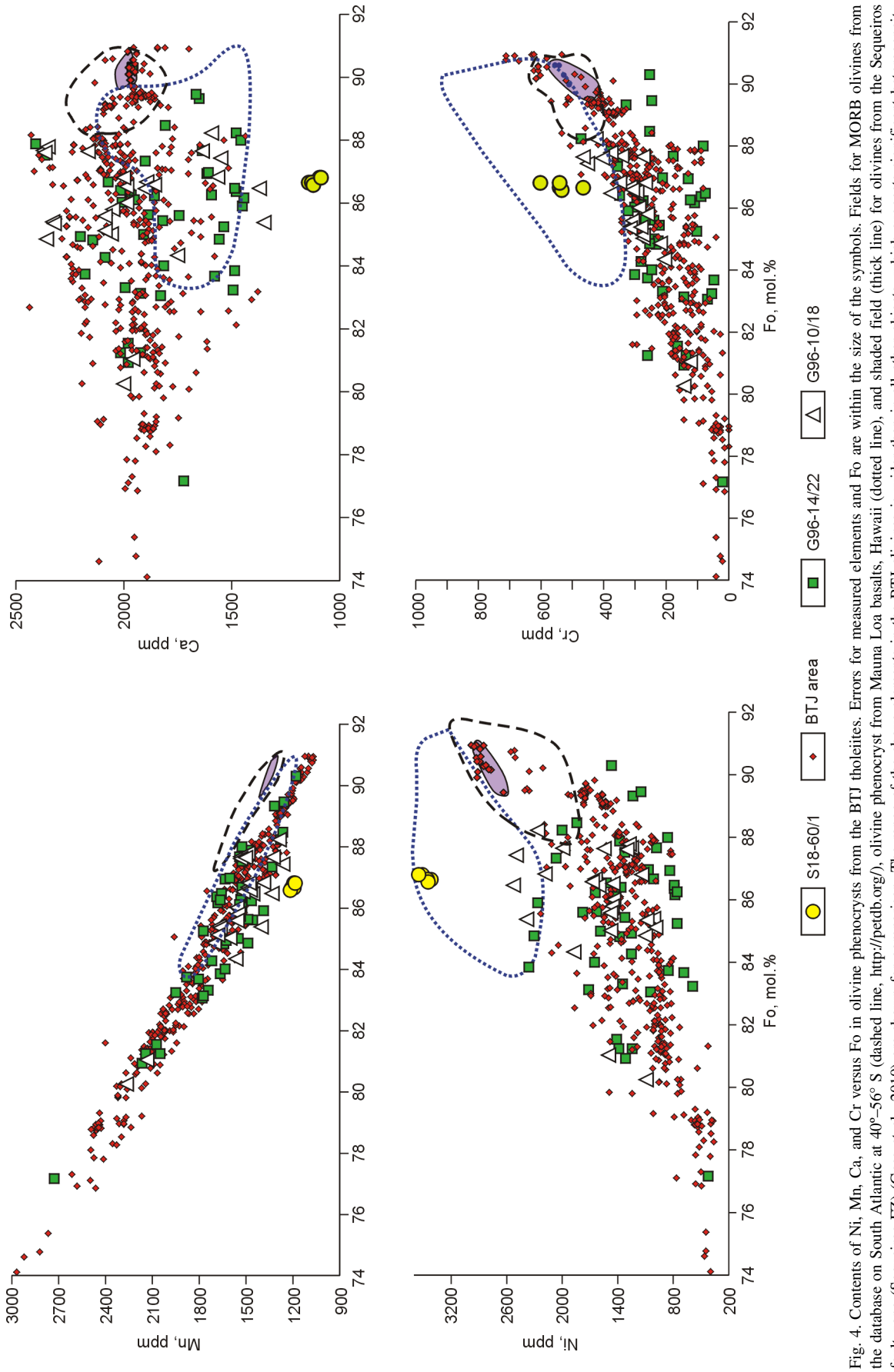

Fig. 4. Contents of Ni, Mn, Ca, and Cr versus Fo in olivine phenocrysts from the BTJ tholeiites. Errors for measured elements and Fo are within the size of the symbols. Fields for MORB olivines from the database on South Atlantic at 40°–56° S (dashed line, http://petdb.org/), olivine phenocryst from Mauna Loa basalts, Hawaii (dotted line), and shaded field (thick line) for olivines from the Sequeiros fault zone (Sequeiros FZ) (Goss et al., 2010) are shown for comparison. The range of the above elements in the BTJ olivines is wider than in all other objects, which suggests significant heterogeneity of crystallizing melts.

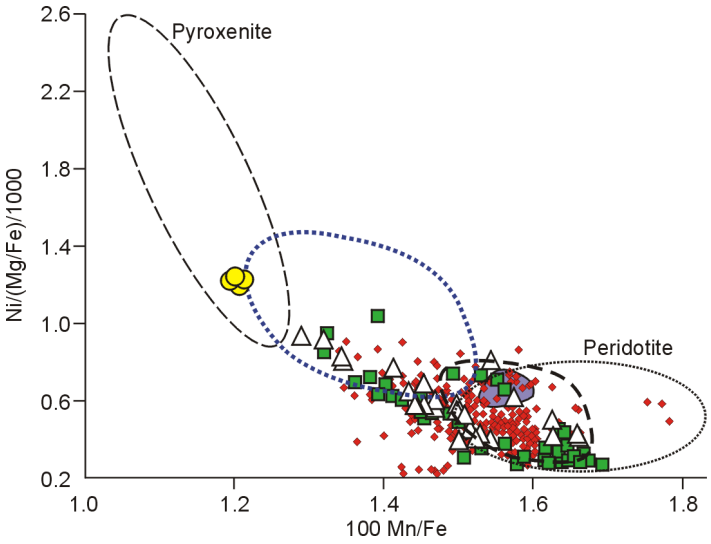

Fig. 5. Ni/(Mg/Fe)/1000 versus 100Mn/Fe in olivine phenocrysts from the BTJ tholeiites. The fields for pyroxenite and peridotite are from Sobolev et al. (2007). The remaining symbols are the same as in Fig. 4.

ites at a given Fo content plot within the array intermediate between olivines crystallized from peridotite-derived melts (field for peridotite with the highest 100Mn/Fe and lowest Ni/(Mg/Fe)/1000) and olivines crystallized from pyroxenite-derived melts (field for pyroxenite with the highest Ni/(Mg/Fe)/1000) and lowest 100Mn/Fe) (Fig. 5, Table 1).

These values were used to calculate the average proportions of pyroxenite-derived melt (X_{Px} Ni = 10.54 · NiO/(MgO/FeO)—0.4368; X_{Px} Mn = 3.483–2.071 · (100 Mn/Fe) (Sobolev et al., 2007)) for each sample and each station in the BTJ area. The results in Table 1 and Fig. 6 show that the proportion of pyroxenite-derived melt (X_{Px} Mn/Fe ≈ 5%) is lowest for samples dredged at stations G96-10, G96-14, S18-29, and S18-32, located in different parts of the SWIR rift valley and Spiess Ridge. The contribution from the pyroxenitic source in samples dredged at station S18-22 from the SWIR rift valley and from the slope of caldera on the summit of the Spiess Ridge (G96-15, S18-16) is usually X_{Px} Mn/Fe = 15–50%.

The largest variation in the proportion of pyroxenite-derived melts (X_{Px} Mn/Fe = 5–80%) was found in samples recovered from st. G96-10, located on a bathymetric high on the western slope of the Spiess Ridge (Fig. 1) and st. G96-14, located on the slope of caldera on the Spiess Ridge. Olivine phenocrysts from tholeiites at st. S18-29 (western slope of the SWIR rift valley) also have wide variations in the proportion of pyroxenite-derived melts (X_{Px} Mn/Fe = 10–60%).

These results clearly indicate the involvement of the pyroxenite source in the generation of the BTJ primary melts. This component is likely to represent either the oceanic crust, recycled in a deep mantle (Hoffmann, 2003) or fragments of the early-formed oceanic crust that underwent melting during a period of ridge jumping (Sushchevskaya et al., 2003). In any case, the transformation of this material into eclogite implies crystallization of mantle rocks with a free SiO_2 phase (Sobolev and Sobolev, 1977).

Unlike the data on MORB olivines, the available data on BTJ olivines are highly heterogeneous. For example, one unusual sample (G96-14/22) used in this study is a dolerite fragment without remnants of quench glass. The composition of phenocrysts is typical of the BTJ tholeiites: Ol + Cpx + (Pl). Concentration ranges of olivine phenocrysts from this sample are as follows (ppm): 77–90 mol.% (Fo), 119–229 (Co), 423–2361 (Ni), 6–370 (Al), 72,960–16,5372 (Fe), 1179–2728 (Mn), 257,550–295,484 (Mg), 1444–2409 (Ca), and 21–472 (Cr). The amount of the pyroxenite component is X_{Px} Mn = 0–0.8, X_{Px} Ni = 0–0.6.

Geochemistry of BTJ melts

The study on the behavior of lithophile elements in the BTJ tholeiites revealed a weak enrichment of melt, which is reflected in the character of their REE distribution patterns (only two samples exhibit strongly depleted patterns) (Sushchevskaya, 1999; Sushchevskaya et al., 2003) (Table 1, Fig. 7*a*). The different BTJ segments demonstrated the overall similarity trace and lithophile element patterns. The BTJ tholeiites show enrichments in Nb and Ta relative to Ba and Rb and depletions in Pb, Rb, and Ba and weak depletions in Th and U. Such lithophile element patterns are similar to those of HIMU basalts (Willbold and Stracke, 2006). The most fractionated compositions from the Spiess Ridge display a pronounced depletion in Sr, probably due to crystallization of plagioclase ($D^{Sr}_{plag/melt} > 1$), which causes a decrease in Sr content of melt, because the Sr partition coefficient for plagioclase is >1. The trace element patterns are characterized by relative enrichment in light and middle rare earth elements (LREE and MREE) relative to heavy rare earth elements (HREE), while the depletion in HREE usually points to the "garnet effect" (which is also supported by $(Gd/Yb)_n > 2.5$).

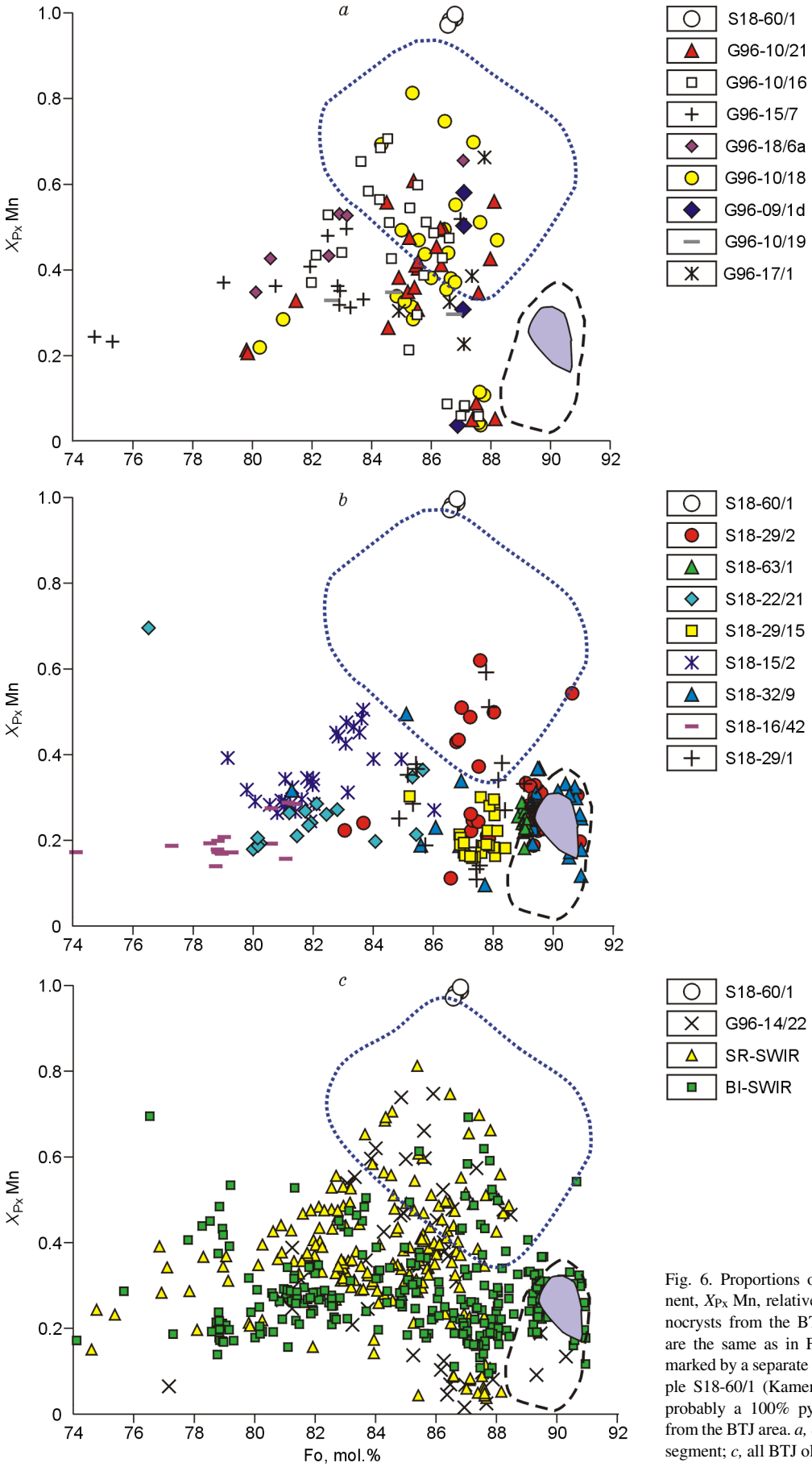

Fig. 6. Proportions of pyroxenitic component, X_{Px} Mn, relative to Fo in olivine phenocrysts from the BTJ tholeiites. Symbols are the same as in Fig. 4; each sample is marked by a separate symbol except *c*. Sample S18-60/1 (Kamenetsky et al., 2001) is probably a 100% pyroxenite-derived melt from the BTJ area. *a,* Spiess Ridge; *b,* SWIR segment; *c,* all BTJ olivines.

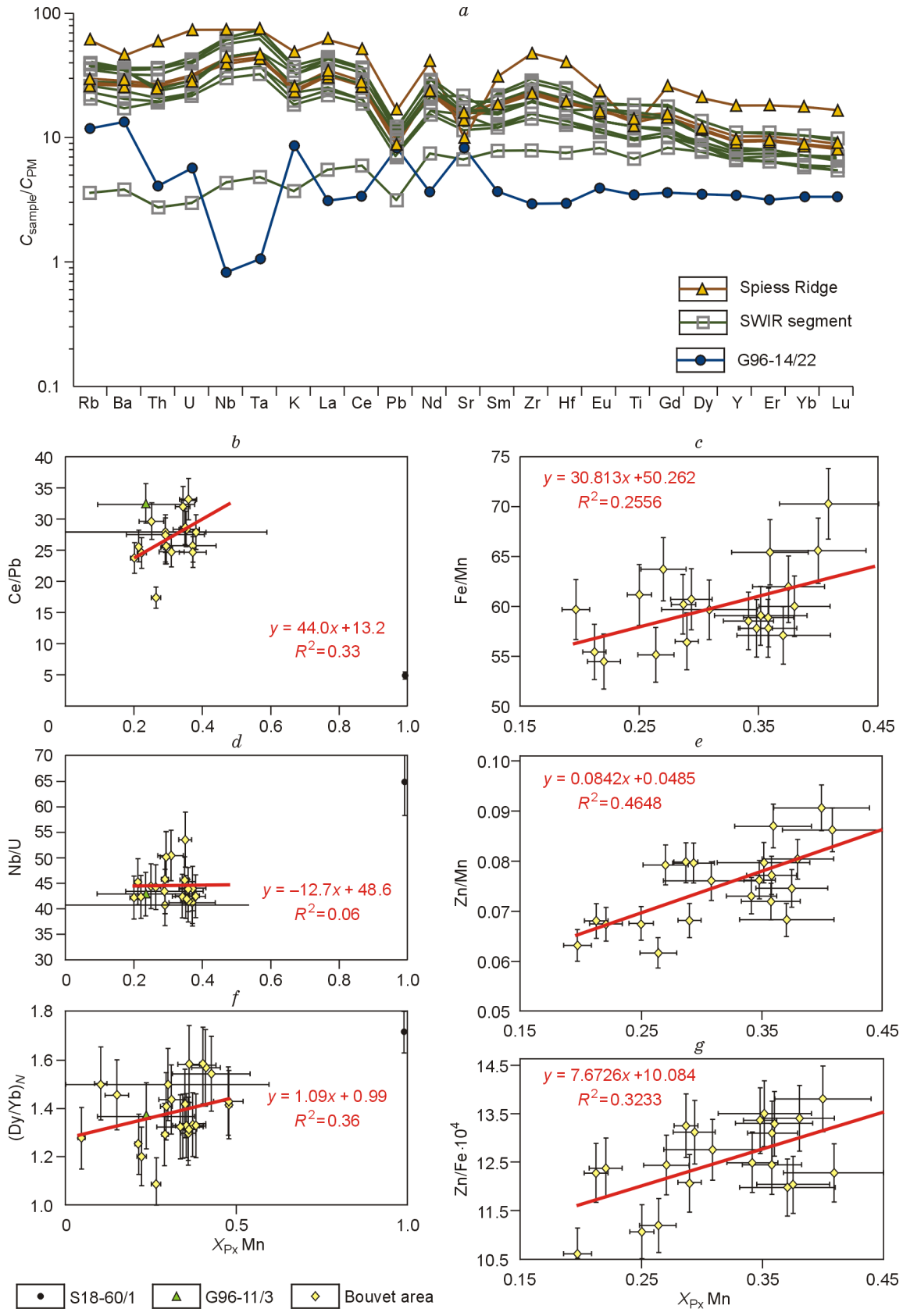

Fig. 7. Geochemical characteristics of tholeiites from the Bouvet triple Junction area. *a*, Lithophile element patterns normalized to primitive mantle after Hoffmann (1988); *b*—*g*, correlations between the proportions of pyroxenitic component, X_{Px} Mn, and tracer incompatible element ratios of BTJ melts. The figure shows average values for each stations.

The REE distribution patterns and $(Gd/Yb)_n$ values suggest the presence of garnet in the source of BTJ melts.

One sample (G96-14/22) demonstrates the highly unusual REE pattern, which is not typical of MORB tholeiites, with a marked Nb–Ta minimum, indicating the contribution of a crustal component in the source region (Ewart et al., 2004).

The character of enrichment of a source for tholeiitic BTJ tholeiites was determined by comparing values of the tracer parameters Ce/Pb, $(Gd/Yb)_n$, Nb/U, Fe/Mn, Zn/Mn, and Zn/Fe (average values for each station) with average values of the pyroxenite component $X_{Px}Mn$ (Fig. 7*b*, *c*). These plots show standard deviations 1σ for X_{Px} Mn and 10% error for the lithophile element ratios. The tracer ratios such as Ce/Pb and $(Gd/Yb)_n$ demonstrate a positive correlation with X_{Px} Mn, which is indicative of the presence of garnet and, thus, pyroxenite in the source of the BTJ melts. The correlation coefficients are $R^2 = 0.38$ for Ce/Pb and $R^2 = 0.32$ for (Gd/Yb)*n*. Therefore, by Pearson criterion, the probability of a statistically random correlation is less than 5%. The Ce/Pb ratio is 25 and may reach 50 at pyroxenite melt fractions of 40%, marking the value of this ratio in possible primary pyroxenite melts.

Zn/Fe, Zn/Mn, and Fe/Mn are constant in melts during partial melting of peridotite, because their partition coefficients $K_{DS\ (Ol,Opx/Melt)}^{Zn/Fe,\ Fe/Mn,\ Zn/Mn}$ are almost equal to 1 (LeRoux et al., 2010, Qin and Hamayun, 2008). Zn/Fe ratios fractionate if garnet and/or clinopyroxene are the main phases in the source during melting due to $D_{(Cpx,\ Gt/Melt)}^{Zn} \ll 1$, producing significant Zn enrichment in the melts. At the same time, Zn/Fe ratio appears not to be fractionated by olivine crystallization and the more evolved melts have the initial Zn/Fe values. Therefore, high Zn/Fe ratios will be indicative of the garnet/clinopyroxene-rich source lithologies (LeRoux et al., 2010). Clear positive correlations between all of the above ratios and pyroxenite component $X_{Px}Mn$ indicate the presence of garnet/clinopyroxene as the main phases in the source of BTJ lavas (Fig. 7*c*). The coefficients of correlation of $Zn/Fe \times 10^4$, Zn/Mn, and Fe/Mn with $X_{Px}Mn$ are $R^2 = 0.32$, 0.47, and 0.26, respectively; they are shown in plots together with standard deviation 1σ for X_{Px} Mn and 10% error for tracer ratios.

Discussion

The new results on the composition of olivine phenocrysts and quench glasses in tholeiites from the BTJ area significantly deepen our understanding of the nature of the primary source for BTJ lavas. The observed compositional heterogeneity of olivines and rocks points to heterogeneity in the primary melts and mantle source. At the same time, no distinct geochemical differences were documented from two major structures of the BTJ area (SWIR and Spiess Ridge). The presence of tholeiites having a different degree of enrichment was documented from various sampling locations throughout the study area.

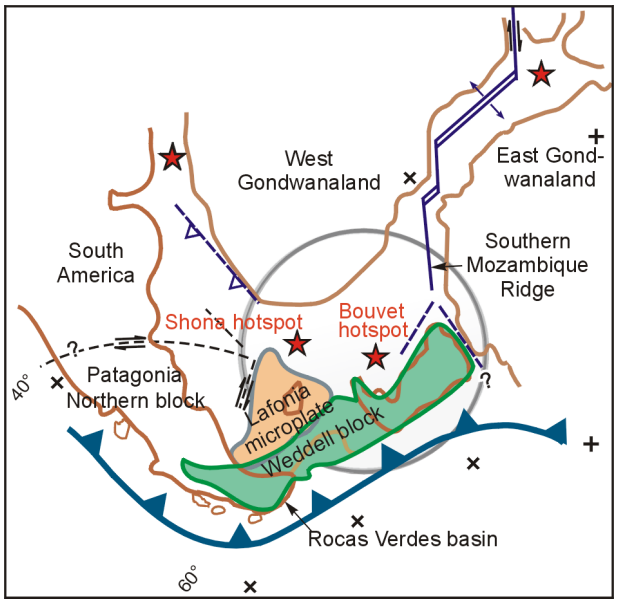

Fig. 8. Reconstruction at ~175 Ma modified after Ben-Avraham et al. (1993). At the early stages (ca. 180170 Ma), the Karoo-Maud plume covered the south-eastern part of Africa and western part of Eastern Antarctica. At present, it covers the area within the Bouvet hotspot. The existence of an ancient island arc around the South Atlantic (blue line) and the formation of microplates (Weddell block and Lafonia) separated by rift zones can be inferred. The modern Shona and Bouvet hotspots (stars) are confined to the area covered by the Karoo-Maud superplume (grey field) originated at about 180 Ma.

The most important result of our study is the first evidence for the existence of substantial heterogeneity in trace element composition and proportions of pyroxenite-derived melts erupted in the BTJ area, which were reflected in the compositional variations within an individual samples and in all dredge stations. This geochemical variation observed in the BTJ area is much larger than in other regions of tholeiitic magmatism in the South Atlantic (Figs. 4, 5, 7). Such compositional variability within the same segment of the sea floor is quite unusual and uncommon.

The compositional variability of BTJ tholeiites can be explained by substantial heterogeneities of the primary melts, which were generated in the mantle source beneath the Bouvet Island segment. It should be emphasized that although the proportions of pyroxenite-derived melt differ in each sample (small-scale heterogeneity), the average values calculated for samples and stations demonstrate significant correlations with the compositions of quench glasses. This is indicative of a large-scale heterogeneity in the mantle source.

The majority of BTJ melts can be classified as enriched tholeiites derived from the enriched source region. This conclusion was earlier confirmed by LeRoex et al. (1982). However, asthenosphere-derived melts typical of mid-ocean ridge tholeiitic magmatism were also documented from the BTJ area. The presence of negative U and Th and positive Nb and Ta anomalies are the most distinct characteristics in terms of the genetic affinity of primary BTJ melts, reflecting their derivation from an uncontaminated mantle source. Another

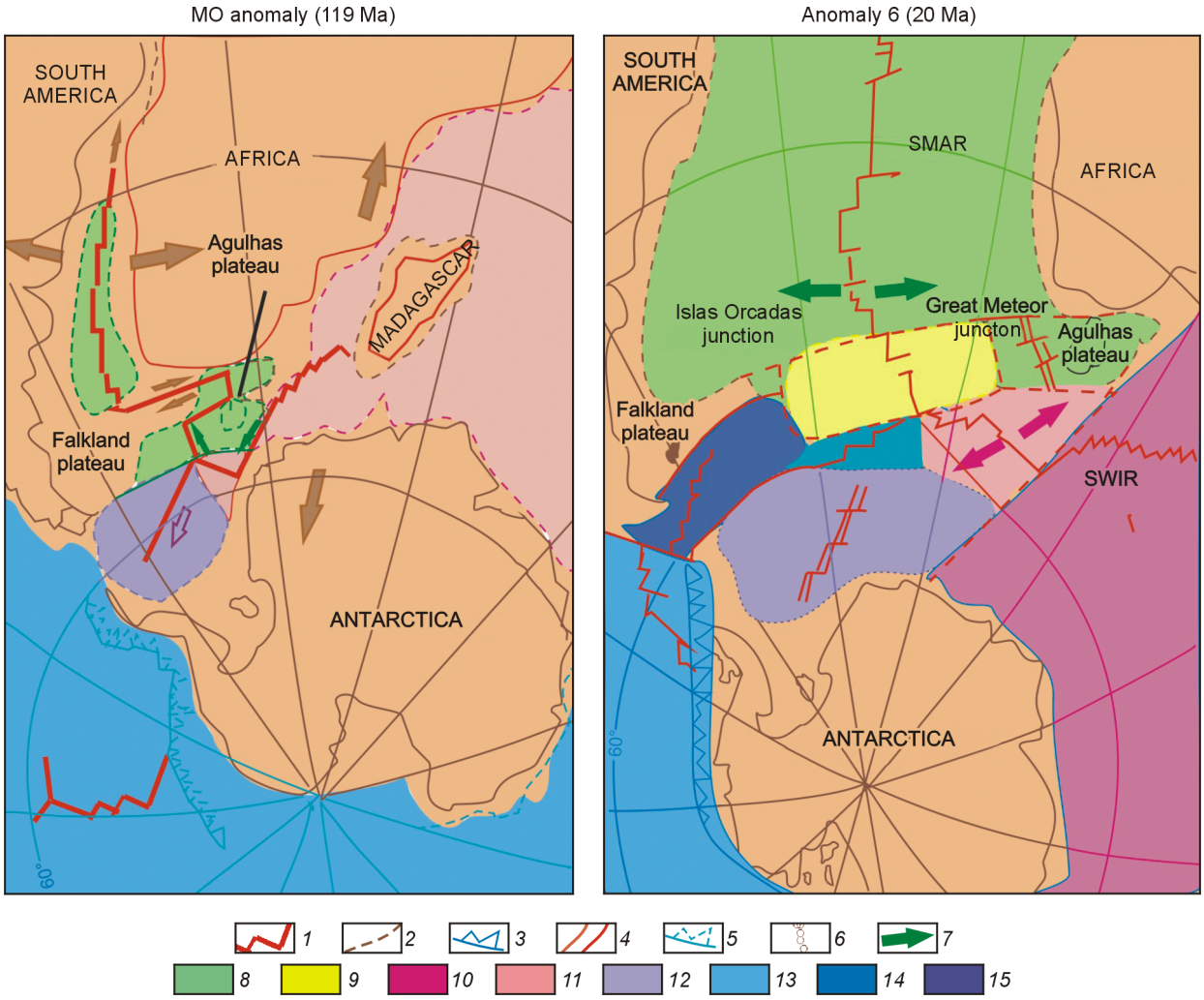

Fig. 9. Reconstruction of plate motions during the breakup of Gondwana and opening of the Southern Ocean, after Lawver et al. (1985), Martin and Hartnady (1986), McCarron and Larter (1998). *1*, modern MORs; *2*, faults and their traces; *3*, subduction zones; *4*, paleorifts; *5*, paleosubduction zones; *6*, junctions; *7*, spreading direction; oceanic crust beneath SMAR (*8*); southern SMAR (*9*); SWIR (*10*); western segment of SWIR (*11*); spreading ridge of the Weddell Sea (*12*); spreading ridges of the Pacific Ocean (*13*); AAR (*14*); *15*, Scotia Plate.

distinctive feature is the overall enrichment of the incompatible trace element patterns of the studied samples (Fig. 7).

The overall depletion in HREE relative to LREE and MREE suggests the presence of garnet in the mantle source. Significant correlations between average proportions of a pyroxenite-derived melt calculated from the compositions of olivine phenocrysts and the characteristic $(Gd/Yb)_n$ ratio in corresponding quench basaltic glasses reflect production of a primary magma by melting of garnet pyroxenite together with peridotite. Additional evidence for the involvement of garnet pyroxenite in the melting of primary magmas is provided by good correlations between major elements ($Zn/Fe \times 10^4$, Zn/Mn, Fe/Mn) and the amounts of pyroxenite-derived melt, on the one hand, and trace element ratios (Ce/Pb, $(Dy/Yb)_n$), on the other hand. A significant correlation between the Ce/Pb ratio and the amount of pyroxenitic melt X_{Px} Mn implies possible contamination of peridotitic melts from the BTJ area by a component with high Ce/Pb values, probably, recycled oceanic crust (Hoffmann, 1988).

We speculate that repeated changes in the geodynamic setting in the BTJ area may have been responsible for this compositionally unusual magmatism. The entire region was formed as a result of the spreading of the Karoo—Maud—Ferrar plume at about 180 Ma, which triggered the final breakup of Gondwana (Figs. 8 and 9). Subsequently, this region underwent a complex evolution, involving the drift of Gondwanan fragments and the formation of new spreading centers.

Three major events were documented in the history of the BTJ area. The first Bouvet triple junction, Bouvet-1 TJ, was formed at approximately 119–124 Ma. The second, Bouvet-2 TJ, was formed at 93–105, and the third, Bouvet-3 TJ, was formed at 25–30 Ma (Dubinin et al., 1999). Lithospheric plates and spreading ridges moved relative to each other, changing their initial positions in space. This dynamics resulted in the melting of early oceanic lithosphere crust, leading to large-scale melt migration. At the same time, the possible influence of subduction zones on the generation of enriched magmas

from the BTJ area cannot be ruled out. Such subduction zones were located at the western boundary (subduction zone at the South Sandwich Islands) and southern boundary (Jane Bank subduction zone) of Scotia Plate (McCarron and March, 1998).

Because the isotope ratios of samples from the BTJ area indicate the involvement of rocks of different genesis and age in melting of BTJ basalts (Migdisova, 2012; Sushchevskaya et al., 1999, 2003), the nature of the pyroxenitic component involved, along with the peridotitic component, in mantle melting is heterogeneous. One sample representing quenched andesitic glass (S18-60/1) with isotope ratios typical of continental crust recycled to the mantle was documented from the BTJ area (Kamenetsky et al., 2001). However, our data show that the geochemical signatures of the studied tholeiites do not support their derivation from melting of a mantle source contaminated by continental crust (Fig. 7). Therefore, the possibilities for the presence of contaminant lithologies of different composition and origin in the source region cannot be ruled out. At the present stage of inbvestigation, we cannot determine with certainty which of the contaminant lithologies involved in melting of the peridotite source of the BTJ rocks is a plume-derived component and which is associated with delamination of the continental or oceanic crust.

Conclusions

1. Tholeiites from the Bouvet triple junction display a wide compositional heterogeneity, which was during the evolution of a particular magmatic system and manifested at different scales, either within each sample or between stations over the entire study area.

2. The heterogeneity of the mantle source for BTJ melts was caused by mixing of a peridotitic component with a pyroxenitic component of different genesis, which may have been derived from the plume source or from ancient oceanic crust or continental lithosphere affected by plume activity.

This study was supported by the Russian Science Foundation (project no. 16-17-10139).

References

Ben-Avraham, Z., Hartnady, C.J.H, Malan, J.A., 1993. Early tectonic extension between the Agulhas Bank and the Falkland Plateau due to the rotation of the Lafonia microplate. Earth Planet. Sci. Lett., 117, 43—58.

Danyushevsky, L.V., Plechov, P., 2011. Petrolog3: Integrated software for modeling crystallization processes. Geochemistry, Geophysics, Geosystems 12 (7), Q07021, doi:10.1029/2011GC003516.

Dickey, J.S., Frey, E.A., Hart, S.R., Watson, E.B., Thompson, G., 1977. Geochemistry and petrology of dredged basalts from the Bouvet triple junction, South Atlantic. Geochim. Cosmochim. Acta 41, 1105–1118.

Douglass, J., Schilling, J-G., Kingsley, R.H., 1995. Influence of the Discovery and Shona mantle plumes on the southern Mid-Atlantic Ridge: Rare earth evidence. Geophys. Res. Lett. 22 (21), 2893–2896.

Dubinin, E.P., Sushchevskaya, N.M., Grokholskii, A.L., 1999. The evolution of spreading ridges of the South Atlantic and spatiotemporal position of the Bouvet Triple Junction. Russ. J. Earth Sci. 1 (5), 423–435.

Ewart, A., Marsh, J.S., Milner, S.C., Duncan, A.R., Kamber, B.S. Armstrong, R.A., 2004. Petrology and Geochemistry of Early Cretaceous Bimodal Continental Flood Volcanism of the NW Etendeka, Namibia. Part 1: Introduction, Mafic Lavas and Re-evaluation of Mantle Source Components. J. Petrol. 45 (1), 59–105.

Fahey, A.J., Zinner, E.K., Crazaz, G., Kornacki, A.S., 1987. Microdistributions of Mg isotopes and REE abundances in a Type A calcium-aluminum-rich inclusion from Efremovka, Geochim. Cosmochim. Acta 51, 3215—3229.

Falloon, T.J., Green, D.H., 1987. Anhydrous partial melting of MORB pyrolite and other peridotite compositions at 10 kbar: Implications for the origin of primitive MORB glasses. Mineral. Petrol. 37, 181–219.

Falloon, T.J., Green, D.H., Harris, K.L., 1988. Anhydrous partial melting of a fertile and depleted peridotite from 2 to 30 kbar and applications to basalt petrogenesis. J. Petrol. 29 (6), 1257–1282.

Goss, A.R., Perfit, M.R., Ridley, W.I., Rubin, K.H., Kamenov, G.D., Soule, S.A., Fundis, A., Fornari, D.J., 2010. Geochemistry of lavas from the 2005–2006 eruption at the East Pacific Rise, 9°46?N–9°56?N: Implications for ridge crest plumbing and decadal changes in magma chamber compositions. Geochem. Geophys. Geosyst. 11, Q05T09, doi: 10.1029/2009GC002977.

Gurenko, A.A., Sobolev A.V., 2006**.** Crust-primitive magma interaction beneath neovolcanic rift zone of Iceland recorded in gabbro xenoliths from Midfell, SW Iceland. Contr. Miner. Petrol. 151, 495–520.

Gurenko, A.A., Sobolev, A.V., Hoernle, Kaj A., Hauff, F., Schmincke, H.-U., 2009. Enriched, HIMU-type peridotite and depleted recycled pyroxenite in the Canary plume: A mixed-up mantle. Earth Planet. Sci. Lett. 277, 514–524.

Herzberg, C., 2006. Petrology and thermal structure of the Hawaiian plume from Mauna Kea volcano. Nature 444, 605–609.

Hofmann, A.W., 1988. Chemical differentiation of the Earth: The relationship between mantle, continental crust, and oceanic crust. Earth Planet. Sci. Lett. 90, 297–314.

Hofmann, A.W., 2003. Sampling mantle heterogeneity through oceanic basalts: isotopes and trace elements, in: Treatise on Geochemistry. Elsevier, Amsterdam, Vol. 2, pp. 61–101.

Jarosevich, E.J., Nelen, J.A., Norberg, J.A., 1980. Reference samples for electron microprobe analysis. Geostandarts Newsletter 4, 43—47.

Jochum, K., Dingwell, D., Rocholl, A., Stoll, B., Hofmann, A., Becker, S., Besmehn, A., Bessette, D., Dietze, H., Dulski, P., Erzinger, J., Hellebrand, E., Hoppe, P., Horn, I., Janssens, K., Jenner, G.A., Klien, M., McDonough, W.F., Maetz, M., Mezger, K., Munker, C., Nikogosian, I.K., Pickhardt, C., Raczek, I., Rhede, D., Seufert, H.M., Simakin, S.G., Sobolev, A.V., Spettel, B., Straub, S., Vincze, L., Wallianos, A., Weckwerth, G., Weyer, S., Wolf, D., Zimmer, M., 2000. The preparation and preliminary characterisation of eight geological MPI-DING reference glasses for in-site microanalysis. J. Geostand. Geoanal. 24, 87–133.

Kamenetsky, V.S., Maas, R., Sushchevskaya, N.M., Norman, M.D., Cartwright, I., Peyve, A.A., 2001. Remnants of Gondwan continental lithosphere in oceanic upper mantle: Evidence from the South Atlantic Ridge. Geology 29 (3), 243–246.

Kleinrock, M.C., Morgan, J.Ph., 1988. Triple junction reorganization. J. Geophys. Res. 93, 2981–2996.

Lawver, L.A., Sclater, J.G., Meinke, L., 1985. Mesozoic and Cenozoic reconstructions of the South Atlantic. Tectonophysics 114, 233–254.

Le Roex, A.P., Dick, H.J.B., Reid, A.M., Erlank, A.J., 1982. Ferrobasalts from the Spiess Ridge segment of the Southwest Indian Ridge, Earth and Planetary. Sci. Lett. 60, 437–451.

Le Roex, A.P., Dick, H.J.B., Reid, A.M., Frey, F.A., Erlank, A.J., 1985. Petrology and geochemistry of basalts from the American-Antarctic Ridge, Southern Ocean: implications for the westward influence of the Bouvet mantle plume, Contrib. Mineral. Petrol. 90, 367–380.

Le Roex, A.P., Dick, H.J.B., Reid, A.M., Frey, F.A., Hart, S.R., 1983. Geochemistry, mineralogy and petrogenesis of lavas erupted along the Southwest Indian Ridge between the Bouvet Triple Junction and 11 degrees East. J. Petrol. 24 (3), 267–318.

Le Roex, A.P., Dick, H.J.B., Watkins, R.T., 1992. Petrogenesis of anomalous K-enriched MORB from the Southwest Indian Ridge: 11°53′ E to 14°38′ E. Contrib. Mineral. Petrol. 110, 253–268.

Le Roux, V., Lee, C.-T.A., Turner, S.J., 2010. Zn/Fe systematics in mafic and ultramafic systems: implications for detecting major element hetero-

geneities in the Earth's mantle. Geochim. Cosmochim. Acta 74, 2779–2796, doi: 10.1016/j.gca.2010.02.004.

Ligi, M., Bonatti, E., Bortoluzzi, G., Carrara, G., Fabretti, P., Penitenti, D., Gilod, D., Peyve, A., Skolotnev, S., Turko, N., 1997. Death and transfiguration of a triple junction in the South Atlantic. Science 276, 243–245.

Ligi, M., Bonatti, E., Bortoluzzi, G., Carrara, G., Fabretti, Pl., 1999. Bouvet triple Junction in the South Atlantic: geology and evolution. J. Geophys. Res. 104 (12), 29,365–29,385.

Martin, A.K., Hartnady, C.J.H., 1986. Plate tectonic development of the South West Indian Ocean: a revised reconstruction of East Antarctica and Africa. J. Geophys. Res. 91, 4767–4786.

McCarron, Joe J., March, R.D., 1998. Late Cretaceous to early Tertiary subduction history of the Antarctic Peninsula. J. Geol. Soc. 155, 255–268.

Migdisova, N.A., 2012. Peculiarities of the Formation of Enriched Tholeiitic Magmas in the Bouvet Triple Junction Area (South Atlantic). Extended Abstract of Cand. Sci. (Geol.-Mineral.) Dissertation. GEOKHI, Moscow.

Migdisova, N.A., Sushchevskaya, N.M., Lattenen, A.V., Mikhal'skii, E.M., 2004. Variations in the Composition of Clinopyroxene from the Basalts of Various Geodynamic Settings of the Antarctic Region. Petrology 12 (2), 206—224.

Nimis, P., Ulmer P., 1998. Clinopyroxene Geobarometry of Magmatic Rocks. Part 1. An Expanded Structural Geobarometer for Anhydrous and Hydrous, Basic and Ultrabasic Systems. Contr. Miner. Petrol. 133, 122—135.

Peyve, A.A., Perfil'ev, A.S., Pushcharovskii, Yu.M., Simonov, V.A., Turko, N.N., Raznitsin, Yu.N., 1995. The Structure of the Southern End of Mid-Atlantic Ridge (the Bouvet Triple Junction). Geotectonics, 1, 40—57.

Peyve, A.A., Turko, N.N., Skolotnev, S.G., Sushchevskaya, N.M., Ligi, M., Fabretti, P., Mazarovich, A.O., Sokolov, S.Yu., Gilod, D.A., 1999. Bouvet Triple Junction: features of structure and evolution, in: Problems of the Lithosphere Geodynamics [in Russian] (Trans. GIN RAS, Issue 511). Nauka, Moscow, pp. 91–109.

Qin, L., Humayun, M., 2008. The Fe/Mn ratio in MORB and OIB determined by ICP-MS. Geochim. Cosmochim. Acta 72, 1660–1677.

Shilling, J.G., Thompson, G., Kinzley, R., Humphris, S.E., 1985. Hotspot-migrating ridge interaction in South Atlantic: geochemical evidence. Nature 313, 187–191.

Simonov, V.A., Peyve, A.A., Kolobov, V.Yu., Milosnov, A.A., Kovyazin, S.V., 1996. Magmatic and hylrothermal processes in the Bouvet triple junction region (South Atlantic). Terra Nova 8, 45–424.

Sobolev, A.V., Hofmann, A.W., Kuzmin, D.V., Yaxley, G.M., Arndt, N.T., Chung, S.-L., Danyushevsky, L.V., Elliott, T., Frey, F.A., Garcia, M.O., Gurenko, A.A., Kamenetsky, V.S., Kerr, A.C., Krivolutskaya, N.A., Matvienkov, V.V., Nikogosian, I.K., Rocholl, A., Sigurdsson, I.A., Sushchevskaya, N.M., Teklay, M., 2007. Published online 28 March 2007. The amount of recycled crust in sources of mantle-derived melts. Science 316, 412–417, doi:10.1126/Science.1138113.

Sobolev, A.V., Hofmann, A.W., Sobolev, S.V., Nikogosian, I.K., 2005. An olivine-free mantle source of Hawaiian shield basalts. Nature 434, 590—597.

Sobolev, V.S., Sobolev, A.V., 1977. The composition of deep-seated pyroxenes and problem of eclogites barrier. Geologiya i Geofizika (12), 46—59.

Sushchevskaya, N.M., Koptev-Dvornikov, E.V., Peyve, A.A., Khvorov, D.M., Belyatsky, B.V., Kamenetsky, V.S., Migdisova, N.A., Skolotnev, S.G., 1999. Peculiaritie4s of crystallization process and geochemistry of tholeiitic magmas from the western segment of the African-Antarctic Ridge (Spiess Ridge) in the Bouvet Triple Junction area. Russ. J. Earth Sci. 1 (3), 221–250.

Sushchevskaya, N.M., Migdisova, N.A., Belyatskii, B.V., Peyve, A.A., 2003. Genesis of enriched tholeiitic magmas in the western segment of the Southwest Indian Ridge, South Atlantic Ocean. Geochem. Int. 41 (1), 1–20.

Willbold, M., Stracke, A., 2006. Trace element composition of mantle end-members: Implications for recycling of oceanic and upper and lower continental crust. Geochem. Geophys. Geosyst. 7 (4), Q04004, doi: 10.1029/2005GC001005.

Zinner, E., Crozaz, G., 1986. A method for the quantitative measurement of rare earth elements in the ion microprobe. Int. J. Mass Spectrom. Ion Processes 69, 17–38.

Editorial responsibility: V.A. Vernikovsky